Library Progress International *Print version ISSN 0970 1052*
Vol.44, No.6, Jul-Dec 2024: P.504-516 *Online version ISSN 2320 317X*

Original Article *Available online at www.bpasjournals.com*

Numerical Analysis of Flowfield around a Hexacopter for the Optimal Placement of an Air Data Sensor

Chang-Hwan Park*[1], Dong-Jin Sheen[2]

Aeronautical System Engineering, Hanseo University, Taean, Chungcheongnam, 32158, Repulblic of Korea

How to cite this article: Chang-Hwan Park, Dong-Jin Sheen (2024). Numerical Analysis of Flowfield around a Hexacopter for the Optimal Placement of an Air Data Sensor. *Library Progress International,* 44(6), 504-516

Abstract

The installation of air data sensors on unmanned aerial vehicles (UAVs) for purposes such as atmospheric and weather observation, as well as UAV positioning in non-GPS environments, has been increasing. This study aims to identify the optimal location for mounting an air data sensor on a hexacopter by analyzing the flow field around it. Potential sensor mounting positions were examined under four flight modes—hovering, ascending, descending, and forward flight—by varying propeller rotation speed, free-stream velocity, and angle of attack. We identified locations along the central line and plane above the hexacopter that meet the allowable velocity error tolerance. The analysis revealed that forward flight mode exhibited the highest velocity error, and that the air data sensor could be mounted at a certain height above the propeller rotation plane.

***Keywords*:** Air Data Sensor, Hexacopter, Sensor Mounting Location, Computational Fluid Dynamics

1. Introduction

Air Data Sensors (ADS), which measure parameters such as wind direction and wind speed, commonly utilize pitot tubes and ultrasonic sensors. A pitot tube measures airspeed by detecting the difference between static and total pressure from incoming airflow during flight, making it highly sensitive to wind direction. Ultrasonic sensors, on the other hand, exploit the principle where sound waves travel faster in the direction of the wind and slower against it. By measuring the time taken for ultrasonic signals to travel from a transmitter to a receiver, wind speed can be calculated [1].

With the rapid growth of the domestic unmanned aerial vehicle (UAV) industry, the application of air data sensors on UAVs has become increasingly common for purposes such as atmospheric and weather observation, as well as determining vehicle positioning in Non-GPS environments. While extensive research has already been conducted to determine the optimal placement of air data sensors on fixed-wing aircraft [2], multirotor drones such as hexacopters present a unique challenge. The interaction between the airflow generated by multiple rotating propellers and free-stream air creates a highly complex flow field around the vehicle. Therefore, selecting an appropriate location for the sensors that minimizes these effects is critical. Theoretically, positioning the sensors as far as possible from the propellers is ideal. However, increasing the distance can lead to added weight and reduced structural stability. Consequently, analyzing the flow field around the multirotor to determine the optimal sensor location is essential [3].

Several studies have attempted to analyze the flow field around multirotor drones. Park et al. [3] performed an unsteady Reynolds Averaged Navier-Stokes (RANS) analysis using an overset grid technique to investigate the flow field around a quadcopter, evaluating measurement errors for different sensor placement positions. Kim et al. [4] conducted a simplified 2D RANS analysis to examine flow characteristics and compared the results with flight test data to propose suitable sensor mounting heights. Kang et al. [5] analyzed the aerodynamic interaction between two propellers by applying a 3D unsteady compressible turbulent flow analysis with a sliding mesh approach, ultimately recommending the optimal propeller separation distance for improved aerodynamic performance. Yoon et al. [6] used Detached Eddy Simulation (DES) to analyze a coaxial multirotor configuration, focusing on the impact of torque on rotor performance.

In this study, as part of the development of an Air Data Test System for a specialized hexacopter, computational fluid dynamics (CFD) analysis was conducted to determine the optimal placement of air data sensors.

2. Flow Analysis

2.1. *Geometry*

The geometry of the aircraft used in this analysis is a hexacopter, as shown in Figure 1, with its specifications listed in Table 1. The propellers used are 22-inch propellers from T-Motor, and precise CAD geometry was obtained through reverse engineering for the analysis.

Figure 1 Hexacopter model

Table 1 Drone Specification

Parameter	**Specification**
Model	**ARTCOPTER RAPTOR GF Hexa 30E**
Weight	**12kg (Battery Included)**
Max Takeoff Weight Recommend	**24kg**
Flight Time	**28min (17kg Takeoff Weight)**
Max Speed	**16m/s**
Size	**1258mm X 1105mm X 383mm**

2.2. *Computational Domain and Grid Generation*

To analyze the flow around the hexacopter, a full-grid test of the entire vehicle should ideally be conducted. However, due to the complexity of the full hexacopter model and the identical design of its six propellers, a grid test was performed on a single propeller to reduce computational time, as illustrated in Fig. 2(a). The computational domain was modeled as a cylindrical shape with a diameter of 20D and a height of 35D, where D represents the propeller diameter.

Grid sensitivity tests were conducted for four conditions by varying the grid size on the propeller surface, as shown in Fig. 2(b). For each condition, the thrust and torque acting on the propeller were calculated by integrating wall pressure and shear stress from converged solutions. The results in Table 2 show that Grid-3 and Grid-4 produced nearly identical values, and Grid-3 was selected as the final grid for this study.

The computational domain for the entire hexacopter model was constructed as a cubic volume centered around the hexacopter. Each edge of the cube was defined as 115 times the propeller diameter D. Boundary conditions were assigned based on flight conditions, including velocity inlet and atmospheric pressure outlet. Ensuring sufficient grid resolution through grid dependency tests is critical to obtaining reliable results in computational fluid dynamics (CFD) analyses. Based on the single-propeller grid tests, grids for the full hexacopter model were generated using ICEM-CFD's Multizone Mesh and Density Mesh techniques, resulting in a final grid size of approximately 75 million cells.

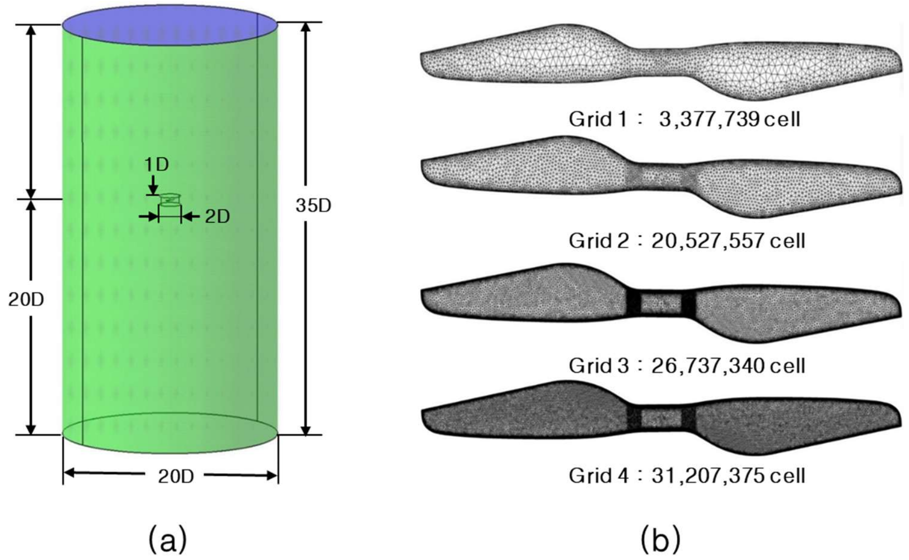

Figure 2 Computational domain and surface grid distribution

Table 2 Comparison of grid test results

Case	Number of cells	Thrust[N]	Torque[Nm]
Grid-1	**3,377,739**	**37.834**	**1.109**
Grid-2	**20,527,557**	**38.234**	**1.064**
Grid-3	**26,737,340**	**38.199**	**1.044**
Grid-4	**31,207,375**	**38.190**	**1.044**

2.3. *Numerical method and Analysis condition*

The CFD simulations were performed using the commercial software ANSYS FLUENT 2020R2. Although some regions near the propeller exhibit characteristics of compressible flow due to high rotational speeds, the majority of the flow can be considered incompressible. Thus, the pressure-based solver in FLUENT was employed to perform Reynolds-Averaged Navier-Stokes (RANS) simulations. The k-ω SST(Shear Stress Transport) turbulence model was used to model turbulent flow. To ensure adequate grid resolution near solid surfaces, the maximum y+ value for the first grid layer was kept below 5. The propeller's rotation was modeled using the Multiple Reference Frame (MRF) technique.

The study considered four flight conditions: hover, ascent, descent, and forward flight. A relative coordinate system was applied, centered on the vehicle, to perform the CFD simulations. The vehicle's flight velocity was replaced by the free-stream velocity for simplicity. A total of 49 simulation cases were analyzed, as summarized in Table 3. The propeller rotational speed was expressed as a rotating speed ratio, defined as the ratio of the actual rotational speed to the maximum rotational speed of the propeller, which was 6,374 rpm in this study.

Table 3 Flow condition

Flight condition	Freestream velocity[m/s]	Rotating speed ratio [%]

Hovering	**0**	**50, 55, 60, 65, 70**
Ascending flight	**-1, -3, -5**	**55, 60**
Descending flight	**1, 3, 5**	**40, 45**
Forward flight	**4, 8, 12, 16, 20, 24 (AOA: -40°, -30°, -20°, -10°)**	**75**
	4, 8, 12, 16, 20 (AOA: 0°)	
	4, 8, 12 (AOA: 10°)	

2.3. *Sensor placement and Velocity error*

In multirotors, air data sensors should be installed at locations where the influence of propeller-induced flow is minimized. To determine the optimal location, CFD simulations were conducted to analyze the flow characteristics at candidate positions. Since the air data sensors must measure the free-stream velocity without distortion, the velocity error at a given position was defined as the difference between the local velocity and the free-stream velocity, as shown below:

Velocity Error=|Local Velocity−Freestream Velocity|

In this study, the pitot tube was assumed to be mounted in the X-direction. The velocity error in the X-direction component (U) was primarily observed. As illustrated in Fig. 3, the sensor was assumed to be mounted on the center axis and the center plane (XZ-plane) of the hexacopter. The forward flight direction of the hexacopter corresponds to the −X direction. The nondimensionalized coordinates X^* and Z^* were defined as the coordinates X and Z normalized by the propeller diameter D. The Z-coordinate was defined with reference to the propeller rotational plane, as shown in Figure 3.

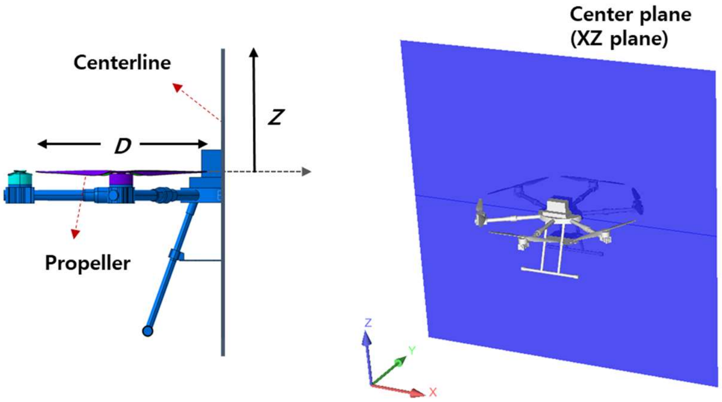

Figure 3 Centerline & center plane

Since no standard specifications currently exist for air data sensors used on multirotors, this study adopted a velocity error threshold based on existing research. For example, outdoor wind measurement systems for meteorological observation have used a wind speed error tolerance of 2 m/s [3,7]. Additionally, the Korea Meteorological Administration's (KMA) standard for automated ground weather stations specifies a wind speed error tolerance of ±0.5 m/s for speeds below 10 m/s and within 5% for speeds above 10 m/s [8]. Based on these references, a velocity error threshold of 1.0 m/s was adopted in this study, with additional investigations conducted for thresholds of 1.5 m/s and

2.0 m/s.

3. Results and Discussion

3.1. *Hover and Ascending Flight*

The hover condition was analyzed for five cases, varying the propeller rotational speed ratio between 50% and 70%. For ascending flight, analyses were conducted at rotational speed ratios of 55% and 60%, with ascent speeds of 1, 3, and 5 m/s. Figure 4 illustrates the velocity magnitude distribution and velocity vector distribution near the propellers during hover and ascending flight. Complex flow patterns caused by the propeller wake are evident below the vehicle during ascent, indicating that sensor placement on the upper part of the airframe is preferable.

Figure 5 shows the U velocity error along Z^* during hover. Across all cases, the error remained within 0.05 m/s, and changes in propeller rotational speed had minimal effect on the velocity error. Figure 6 presents the U velocity error under ascending flight conditions, where solid lines represent a rotational speed ratio of 55%, and dashed lines represent 60%. Similar to the hover condition, U velocity errors were within 0.1 m/s, demonstrating minimal sensitivity to changes in rotational speed.

Figure 7 displays iso-contours of the 1 m/s velocity error on the central plane defined in Figure 3. These contours represent regions where velocity errors are below (outside) or above (inside) 1.0 m/s. For both hover and ascending flight, sensors can be mounted within approximately 90° of the center axis at $Z^* \leq 1.2$ and without angular restrictions at higher Z^*values.

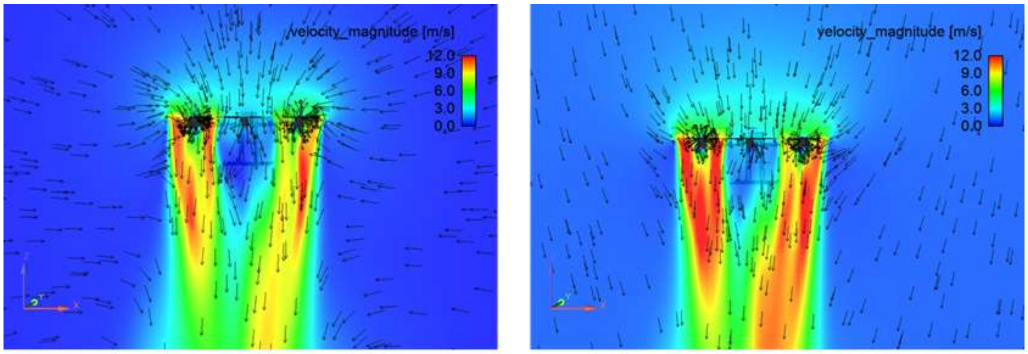

(a) Hovering **b) Ascending flight**

Figure 4 Velocity magnitude and Velocity vector distribution (rotating speed ratio=55%)

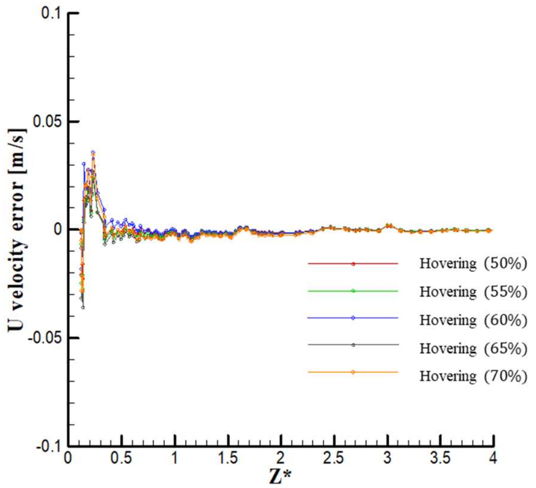

Figure 5 U error distribution (Hovering)

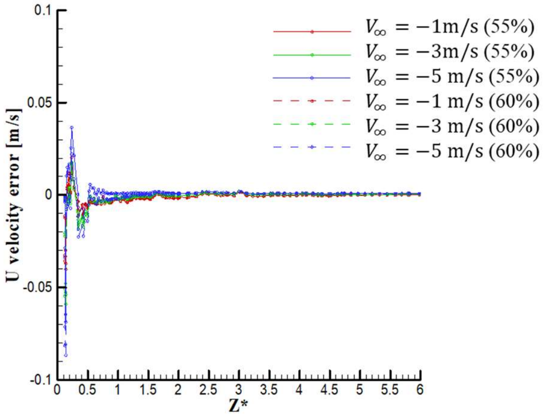

Figure 6 U error distribution (Ascending flight)

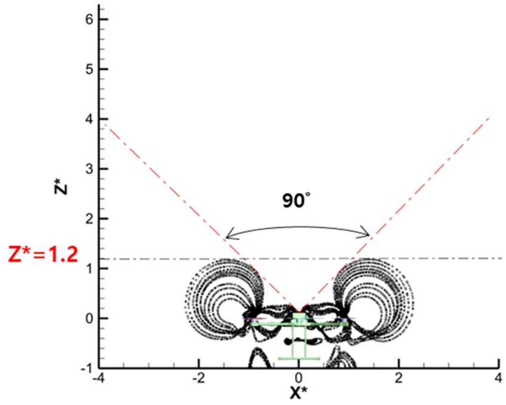

Figure 7 Possible ADS mounting location(hovering & ascending flight)

3.2. *Descending Flight*

Descending flight conditions were analyzed for rotational speed ratios of 40% and 45%, with free-stream velocities of 1, 3, and 5 m/s. Figure 8 shows the velocity magnitude distribution and velocity vector field for a rotational speed ratio of 45% and a free-stream velocity of 5 m/s. In descending flight, interactions between upward airflow induced by descent and the propeller wake create more complex flow patterns compared to hover and ascending flight.

Figure 9 presents the U velocity error along the centerline, which remained within 0.3 m/s for all cases. However, Figure 10 shows significant errors in the W velocity component, which increased with descent velocity. These results align with prior studies, such as Park et al. [3], which identified similar trends when analyzing only the propeller without the airframe. This study incorporated the airframe, demonstrating the mitigating effect of the airframe on upward airflow.

Figure 11 illustrates iso-contours of the 1 m/s velocity error for descending flight on the central plane. The closed contours indicate regions where errors exceed 1 m/s. Across the six descending flight cases, the region satisfying the error threshold of 1 m/s is limited to approximately 34° from the centerline on the central plane. This restriction highlights the increased complexity of descending flight compared to hover and ascending flight.

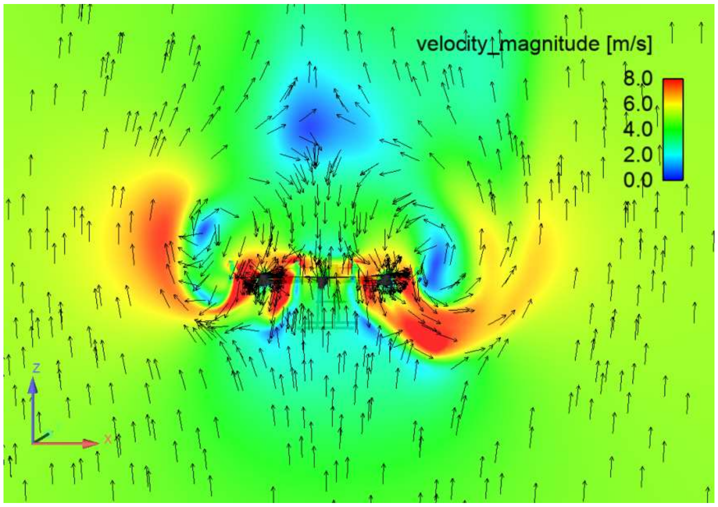

Figure 8 Velocity magnitude and velocity vector distribution (45%, 5m/s)

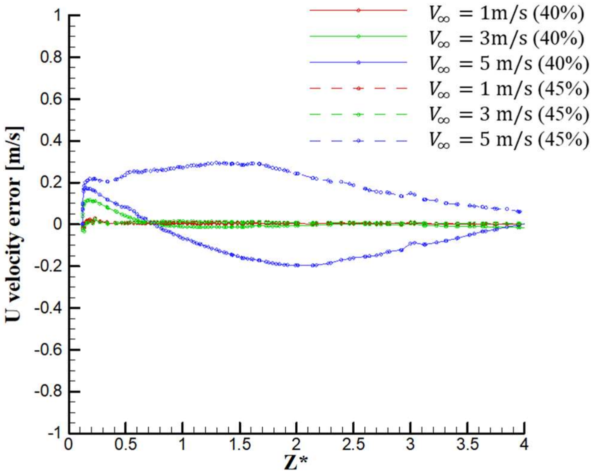

Figure 9 U error distribution (Descending flight)

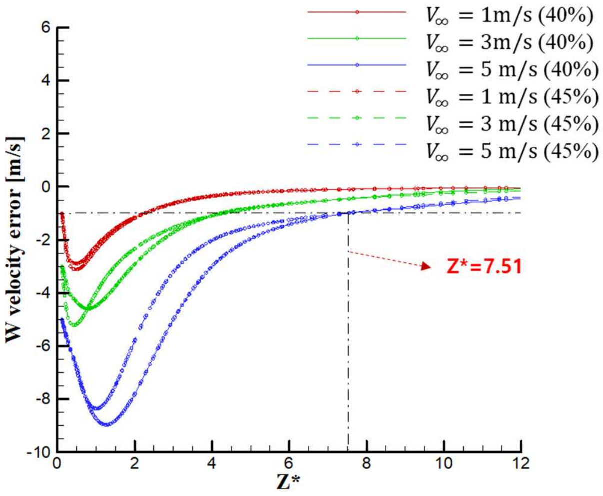

Figure 10 W error distribution (Descending flight)

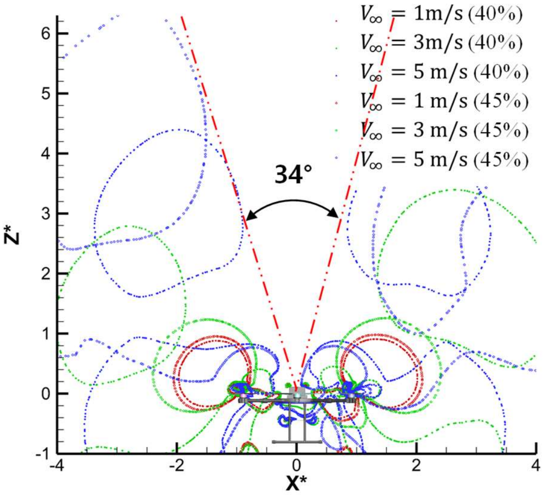

Figure 11 Possible ADS mounting location(descending flight)

3.3. *Forward Flight*

Forward flight conditions were analyzed with a fixed propeller rotational speed ratio of 75%, varying free-stream velocities from 4 to 24 m/s and angles of attack from -40° to +10° across 32 cases. Figure 12 compares the velocity distributions and vector fields for free-stream velocities of 16 m/s at angles of attack of -40° and -10°. Figure 13 shows the same for an angle of attack of -20° with free-stream velocities of 8 and 24 m/s. As the angle of attack or free-stream velocity increases, the wake angle approaches the horizontal axis.

Figure 14(a) shows the UUU velocity error along the centerline for an angle of attack of -30°, where larger free-stream velocities lead to greater errors at lower heights, but these differences diminish at higher altitudes. For the maximum free-stream velocity of 24 m/s, the minimum sensor mounting height is $Z^* = 1.93$. Figures 14(b) and 14(c) show U velocity errors for angles of attack of -10° and +10°, with minimum mounting heights of $Z^* = 2.00$ and $Z^* = 2.17$, respectively. Despite the lower maximum free-stream velocity of 12 m/s for +10°, the velocity error is relatively high.

Figure 15 presents iso-contours of regions exceeding a 1 m/s velocity error on the central plane during forward flight. As free-stream velocity increases, the error regions shift to the right side of the vehicle. Unlike hover, ascending, and descending flight, where mounting locations are primarily determined by angular restrictions, forward flight conditions primarily depend on $Z^* = 1.93$. Across the considered forward flight cases, sensors can be mounted at $Z^* \geq 2.33$ regardless of angle.

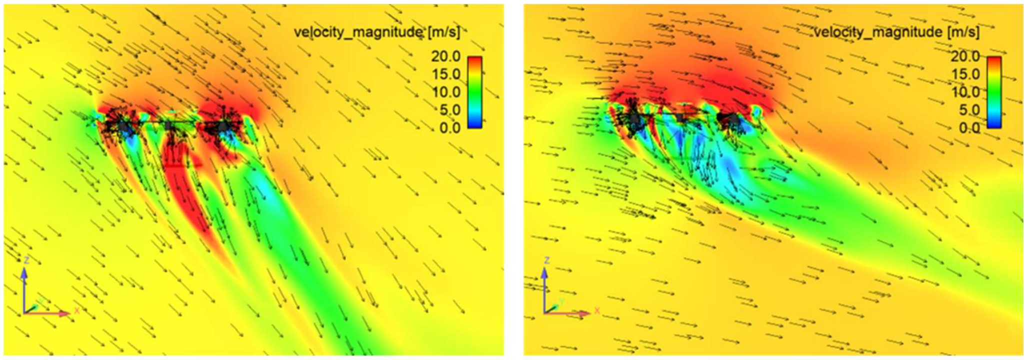

(a) AOA=-40°, V_∞=16m/s (b) AOA=-40°, V_∞=16m/s

Figure 12 Velocity and Vector distribution (V_∞=16m/s, Forward flight)

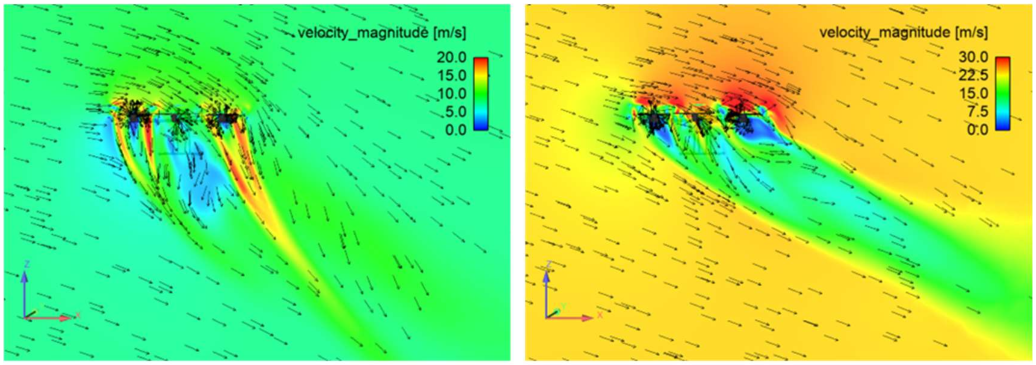

(a) AOA=-20°, V_∞=8m/s (b) AOA=-20°, V_∞=24m/s

Figure 13 Velocity and Vector distribution (AOA=-20˚, Forward flight)

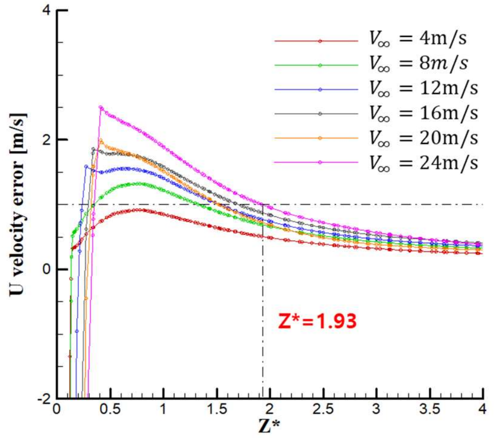

(a) AOA=-30°

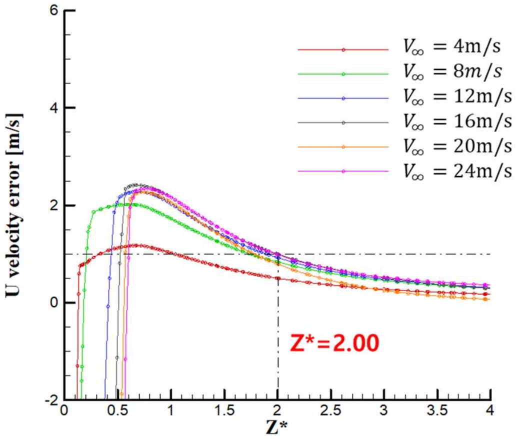

(b) AOA=-10°

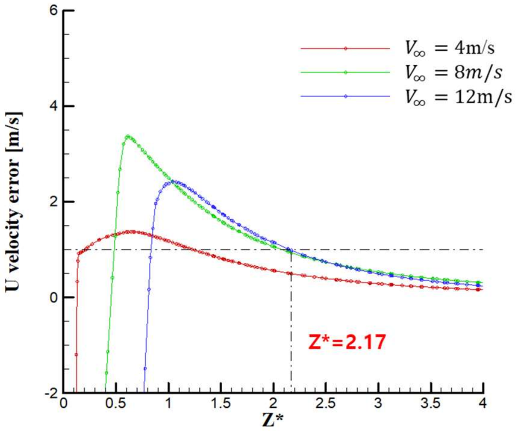

(c) AOA=10°

Figure 14 Velocity error distribution (forward flight)

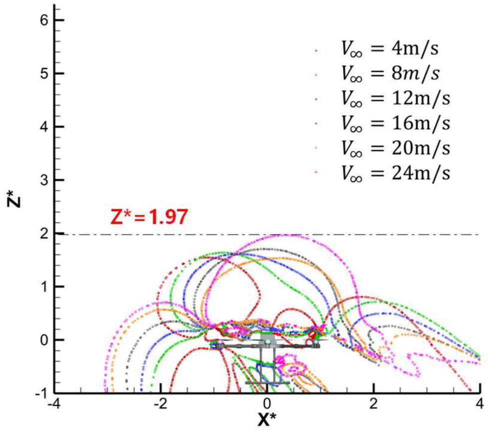

(a) AOA=-30°

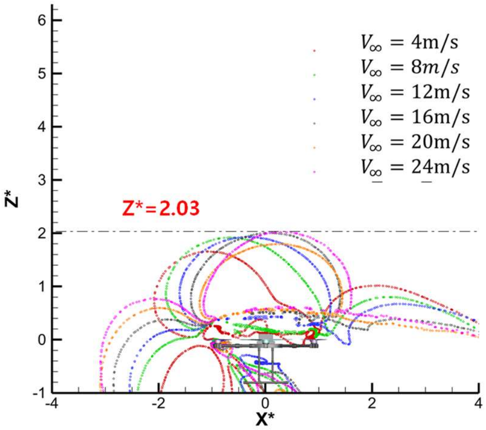

(b) AOA=-10°

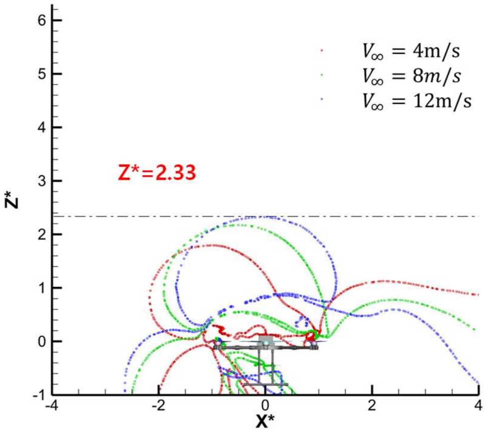

(c) AOA=10°

Figure 15 Possible ADS mounting location (forward flight)

3.4. *Summary of Results*

For hover, ascending, and descending flight conditions, all positions along the centerline satisfied the velocity error threshold of 1.0 m/s. Figure 16 summarizes the minimum allowable sensor mounting height for forward flight, based on thresholds of 1.0 m/s, 1.5 m/s, and 2.0 m/s across various angles of attack. The minimum height was highest for an angle of attack of +10°, with allowable mounting locations at$Z^* = 1.93, 1.68\ and\ 1.38$, respectively, depending on the error threshold. Table 4 converts the nondimensionalized Z^*values to actual heights Z.

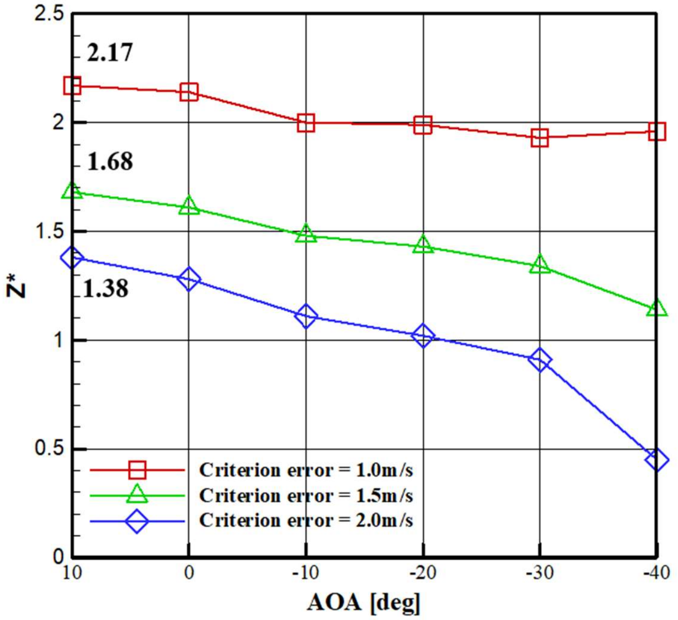

Figure 16 Comparison of the minimum mounting height for sensors based on changes in error criteria

Table 4 Minimum mounting height of ADS

Error Criterion [m/s]	**Z^***	**Z [m]**
1.0	**2.17**	**1.21**
1.5	**1.68**	**0.94**
2.0	**1.38**	**0.77**

4. Conclusion

Through computational fluid dynamics (CFD) analysis of the flow around a hexacopter, this study determined feasible mounting locations for air data sensors. Four flight conditions—hover, ascending, descending, and forward flight—were analyzed by varying free-stream velocity, angle of attack, and propeller rotational speed. The analysis focused on identifying locations on the vehicle's centerline and central plane that satisfied velocity error thresholds for the X-direction component (U).

Hover, ascending, and descending flights showed negligible velocity errors across all positions. Forward flight exhibited relatively higher errors, with allowable mounting heights determined by specific error thresholds. For hover, ascending, and descending flight, sensors could be mounted within specific angular ranges without height restrictions, while forward flight required a minimum height for error tolerance.

5. Acknowledgment

This study was supported by a 2022 research grant from Hanseo University.

6. References

1. Abichandani, P., Lobo, D., Ford, G. Bucci, D. and Kam, M., “Wind measurement and simulation techniques in multi-rotor small unmanned aerial vehicles,” IEEE Access, vol. 8, 2020, pp. 54910-54927.Settles G. S., & Dodson L. J. (1994). Supersonic and hypersonic shock/boundary-layer interaction database. *AIAA journal*, 32(7), 1377-1383.
2. Jeong, W. G., Ju, J. S., Kim, H. U., Hwang, Y. S. and Kim, C. H., “On the selection of ADS(Air Data Sensor) location using CFD,“ Proceeding of The Korean Society for Aeronautical and Space Sciences Fall Conference, November 2008, pp. 175~178.Smits A. J., & Muck K. C. (1987). Experimental study of three shock wave/turbulent boundary layer interactions. *Journal of Fluid Mechanics*, 182, 291-314.
3. Park, Y. M., Lee, C. H. and Lee, Y. G., “Numerical Analysis of Flowfield around Multicopter for the Analysis of Air Data Sensor Installation," Journal of The Korean Society for Aeronautical and Space Sciences, Vol. 11, No. 5, 2017, pp. 20~27.ANSYS FLUENT 2019R3, Theory & User guide
4. Kim, Y. I., Ku, S. K. and Park, C. H., “Flow Analysis and Flight Experiment for Optimum Height of Weather Data Sensor,” Journal of Advanced Navigation Technology, Vol. 22, No. 6, 2018, pp. 551~556.Shih T. H., Liou W. W., Shabbir A., Yang Z., & Zhu J. (1995). A new k-ϵ eddy viscosity model for high Reynolds number turbulent flows. *Computers & fluids*, 24(3), 227-238.
5. Kang, H. J., “NUMERICAL ANALYSIS OF AERODYNAMIC INTERACTIONS IN HOVER FOR THE SEPARATION DISTANCE BETWEEN TWO PROPS,” Journal of Computational Fluids Engineering, Vol. 25, No. 3, 2020, pp. 95~101.Menter F. (1993). Zonal two equation k-ω turbulence models for aerodynamic flows. *In 23rd fluid dynamics, plasmadynamics, and lasers conference* (p. 2906).
6. Yoon, S., Chan, W. M., and Pulliam, T. H., “Computations of Torque-Balanced Coaxial Rotor Flows,” 55th AIAA Aerospace Sciences Meeting, January
7. Kim, J. W., “Development of a Real-Time Weather Observation System with Integrated Sensors and Imaging System for Small Unmanned Aerial Vehicles”, SASE 2017 Spring Conference
8. “Standard Specifications for Automated Weather Observation Equipment”, Korea Meteorological Administration